

Approximate inverse mappings in DC resistivity problems

Yaoguo Li and Douglas W. Oldenburg

Department of Geophysics and Astronomy, University of British Columbia, 2219 Main Mall, Vancouver, Canada V6T 1Z4

Accepted 1991 November 11. Received 1991 November 1; in original form 1991 April 26

SUMMARY

In an E-SCAN DC resistivity experiment a large amount of common source pole–pole potential data from many sources over a pre-designed survey grid are collected. The large number of DC potentials and the spatial configuration in which they are collected invite the development of new imaging and inversion methods. We present three one-pass inversion algorithms. They are based upon the linearized equation for the DC potential under the Born approximation and the assumption that the conductivity model consists of perturbations to a uniform background conductivity. Two algorithms are presented for imaging and inverting for 2-D conductivity models. The first is based upon the theory of charge accumulation in the DC resistivity experiment, in which a sparse representation of the accumulated charge densities due to all current sources is recovered so as to image the structural boundaries. The second method inverts directly for an approximate conductivity model having a minimum structure. Both methods employ linear programming techniques. For 3-D problems, a fast algorithm is developed using a convolutional representation of the surface pole–pole apparent resistivity. It decomposes the 3-D inverse problem into a sequence of 1-D inversions in the wavenumber domain. These 1-D problems are independent of each other and can be solved efficiently. The final spatial domain conductivity model is obtained by inverse Fourier transforming. Despite the Born approximation, this algorithm seems to work for large conductivity contrasts and a certain amount of near-surface variation in conductivity. All algorithms are tested on synthetic data but we also present results from the 3-D inversion applied to field data.

Key words: conductivity, imaging, inversion.

INTRODUCTION

In a typical E-SCAN DC resistivity experiment, ~ 100 electrodes are planted according to a pre-designed grid over the target area. Each electrode is used as a current electrode, and when activated, the potentials are measured at the remaining electrodes. The typical E-SCAN data set therefore consists of multiple groups of common source pole–pole potentials with the total number of data being $\sim 10\,000$. The large number of measured potentials, and the grid arrangement on which those data were collected, offer new opportunities for the development of processing and inversion algorithms. In this paper we present some of these techniques.

Our emphasis is on one-pass algorithms whose output may be of sufficient quality to answer a specific geologic question. The output may be a structural image or it may be a first approximation to the true subsurface distribution of conductivity. Although such a result cannot be considered an acceptable model in that it reproduces the field observations after being input to a rigorous forward modelling, it may contain the necessary information to define the existence or non-existence of a conductive target or to determine an approximate depth of burial or geometric attitude of the body. As such it is useful. In addition, the approximate inversion result can be used as the input conductivity for a more rigorous iterative inversion, or the approximate inverse mapping itself can be iteratively used to find a model which provides an acceptable fit to the data. These attributes have motivated our research on approximate inverse mappings.

The techniques developed here depend upon the dimension of the presumed conductivity model. Geo-electrical structures are always 3-D but if there is a preferred strike direction and if the bodies are sufficiently elongated, then interpretations based upon 2-D equations may be valid. We present two approximate mappings that make explicit use of 2-D geometry. The first

mapping is based upon a physical understanding of charge density in DC resistivity problems (e.g. Alfano 1959; Kaufman 1985; Li & Oldenburg 1990). Charge is accumulated at an interface separating regions of differing conductivity and the relationship between the accumulated charge and the measured potentials is governed by Coulomb's equation. This is a linear relationship and hence invites the use of a linear inverse method to recover the subsurface charge from the measured potentials. Potentials from each current location can be inverted to provide an image of the subsurface charge accumulation and various images can be combined to provide the locations of the conductivity contrasts. The technique has the possibility for outlining the shape of the body.

Rather than combining results from individual inversions, the 2-D problem can be reformulated so that potentials from multiple current electrodes are inverted simultaneously. The output is a conductivity structure rather than a charge accumulation image. As such, it is more closely affiliated to an inversion than to an image. This has an advantage, but the sacrifice made is in the increased computations required.

Most often, however, a 3-D solution is required. Although the 2-D approximate methods are potentially extendable into a higher dimension, the increased computations can make the problem intractable on present-day workstations. For the 3-D problem, we propose an alternative method which explicitly uses the array of E-SCAN data. Field data are Fourier transformed and a sequence of 1-D linear inverse problems is solved in the wavenumber domain. The wavenumber inversions are inverse Fourier transformed to yield the approximation to the true 3-D conductivity structure.

Our paper proceeds by developing the basic approximate equation which linearly relates the measured surface potential data to the subsurface conductivity. The equation is based upon the Born approximation. Variations of this equation are used in all of our imaging and inversion algorithms. We next develop our algorithms and apply them to synthetic data sets. The first 2-D algorithm developed outputs an image of the major charge accumulation; the second algorithm generates an approximate 2-D conductivity. The remainder of the paper is concerned with the 3-D problem. The results of applying the 3-D inverse mapping to synthetic data and to a set of E-SCAN field data are given.

BORN EQUATION FOR DC RESPONSES

Let $\sigma(\mathbf{r})$ be the conductivity structure in a lower half-space V whose upper surface is flat. The potential on the surface resulting from a point source of strength I placed on the surface can be expressed as (e.g. Snyder 1976; Li & Oldenburg 1991)

$$\varphi(\mathbf{r}_{\text{obs}}) = \frac{I}{2\pi |\mathbf{r}_s - \mathbf{r}_{\text{obs}}| \sigma_s} + \frac{1}{2\pi} \int_V \frac{\nabla \sigma(\mathbf{r}) \cdot \nabla \varphi(\mathbf{r})}{\sigma(\mathbf{r}) |\mathbf{r} - \mathbf{r}_{\text{obs}}|} dv, \quad (1)$$

where \mathbf{r}_s and \mathbf{r}_{obs} are the source and observation point respectively, and $\sigma_s = \sigma(\mathbf{r}_s)$. We choose a Cartesian coordinate system with origin at the surface and z positive down. The integral in equation (1) represents the secondary potential which contains all the information about conductivity anomalies and is denoted by

$$\varphi_s(\mathbf{r}_{\text{obs}}) = \frac{1}{2\pi} \int_V \frac{\nabla \sigma(\mathbf{r}) \cdot \nabla \varphi(\mathbf{r})}{\sigma(\mathbf{r}) |\mathbf{r} - \mathbf{r}_{\text{obs}}|} dv. \quad (2)$$

Let the conductivity be represented by $\sigma(\mathbf{r}) = \sigma_0 \mu(\mathbf{r})$. Here σ_0 is the conductivity of a uniform background and $\mu(\mathbf{r})$ is a dimensionless function of spatial position \mathbf{r} . Substituting into (2) yields

$$\varphi_s(\mathbf{r}_{\text{obs}}) = \frac{1}{2\pi} \int_V \frac{\nabla \ln \mu(\mathbf{r}) \cdot \nabla \varphi(\mathbf{r})}{|\mathbf{r} - \mathbf{r}_{\text{obs}}|} dv. \quad (3)$$

Equation (3) is basically Coulomb's equation with the volumetric charge density (scaled by $2\epsilon_0$) represented by the numerator. The charge density is non-zero whenever there is a component of the electric field parallel to the gradient of the conductivity. It is positive when the current flows from a conductive to a resistive region; otherwise, it is negative.

The potential $\varphi(\mathbf{r})$ is not known, but if the deviation of the conductivity from the background is small over the entire model, and if the surface conductivity is equal to σ_0 (thus $\sigma_s = \sigma_0$), we can apply the Born approximation by replacing $\varphi(\mathbf{r})$ in equation (3) with the primary potential

$$\varphi_p(\mathbf{r}) = \frac{I}{2\pi |\mathbf{r} - \mathbf{r}_s| \sigma_0}.$$

We obtain

$$\varphi_s(\mathbf{r}_{\text{obs}}) = \frac{I}{4\pi^2 \sigma_0} \int_V \left(\nabla \ln \mu(\mathbf{r}) \cdot \nabla \frac{1}{|\mathbf{r} - \mathbf{r}_s|} \right) \frac{1}{|\mathbf{r} - \mathbf{r}_{\text{obs}}|} dv. \quad (4)$$

This is a Fredholm equation of the first kind with the conductivity perturbation $\ln \mu(\mathbf{r})$ as the unknown function. Physically, equation (4) approximates the actual secondary potential by considering only the charge accumulation arising from the primary field. The internal interaction of the accumulated charges is neglected.

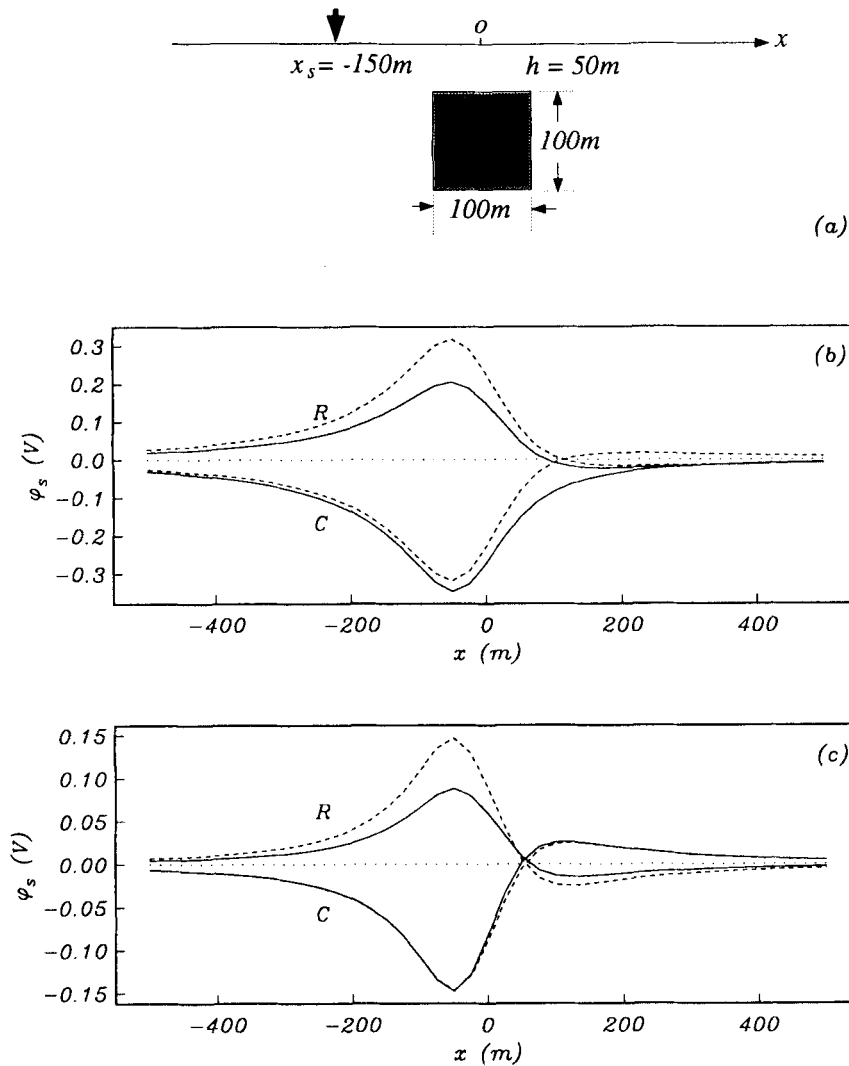


Figure 1. The comparison of the true and the Born approximation potentials over 2-D and 3-D prisms are shown in panels (b) and (c) respectively. The two prisms have the identical cross-sections, as shown in panel (a), and are embedded in a uniform half-space of 0.01 S m^{-1} . The conductivity contrast between the prism and the half-space is 10. The solid lines are the true secondary potentials. The dashed lines represent the potentials from the Born approximation. Curves labelled C and R correspond to conductive and resistive prisms respectively.

Because equation (4) is basic to our algorithms it is important to have some feeling for its validity. We attempt to quantify this for a simple geologic situation in which a conductive or resistive prism is buried in a half-space. The geologic model and electrode geometry is shown in Fig. 1(a). The true secondary potentials and those evaluated from (4) are given in Fig. 1(b) for a 2-D prism and in Fig. 1(c) for a 3-D prism. Generally the shape of the Born potential is very similar to that of the true potential but the amplitude can be significantly different. The Born potentials are greater than the true potentials for a resistive prism and smaller than the true potential for a conductive prism. Amplitude discrepancies of 30 per cent are noted. There are also sign differences. For a conductive 2-D prism the true secondary potential is entirely negative but the Born solution shows a positive side lobe. Interaction between charges reduces the positive charge on the far side of the prism and keeps the potential negative. Overall, however, the agreement between the true and Born potentials is quite good. In fact, the correspondence for the 3-D conductive prism is excellent. This provides optimism that analyses carried out using equation (4) will yield useful results.

APPROXIMATE 2-D IMAGING AND INVERSION

In the case where the anomaly due to a geological structure has a preferred strike and it is sufficiently elongated, the 2-D approximation may be valid. Even though the Born approximation may be somewhat more inaccurate for the 2-D models compared to a 3-D model, from a computational viewpoint there are benefits to using a 2-D formalism if it is possible. For a 2-D structure, $\mu(\mathbf{r}) = \mu(x, z)$. Substituting this into equation (3) and recognizing that terms involving $\mu(\mathbf{r})$ are independent of

variable y , we can carry out the integration with respect to y and obtain

$$\varphi_s(\mathbf{r}_{\text{obs}}) = \frac{I}{4\pi^2\sigma_0} \int_{xz} \left[\frac{\partial \ln \mu(x, z)}{\partial x} (x - x_s) + \frac{\partial \ln \mu(x, z)}{\partial z} z \right] g_a(\mathbf{r}; \mathbf{r}_{\text{obs}}, \mathbf{r}_s) dx dz, \quad (5)$$

where $\mathbf{r}_{\text{obs}} = (x_{\text{obs}}, y_{\text{obs}}, 0)$, $\mathbf{r}_s = (x_s, y_s, 0)$ and the kernel function g_a is

$$g_a(\mathbf{r}; \mathbf{r}_{\text{obs}}, \mathbf{r}_s) = \int_{-\infty}^{\infty} \frac{1}{[(x_{\text{obs}} - x)^2 + (y_{\text{obs}} - y)^2 + z^2]^{1/2}} \frac{1}{[(x_s - x)^2 + (y_s - y)^2 + z^2]^{3/2}} dy.$$

Performing the integration for the special case $y_s = y_{\text{obs}}$ yields

$$g_a(\mathbf{r}; \mathbf{r}_{\text{obs}}, \mathbf{r}_s) = \begin{cases} \frac{2}{\eta_{\text{obs}}\eta_s^2(\eta_{\text{obs}}^2 - \eta_s^2)} [\eta_{\text{obs}}^2 E(s) - \eta_s^2 K(s)], & \eta_{\text{obs}} > \eta_s, \\ \frac{2}{\eta_s(\eta_{\text{obs}}^2 - \eta_s^2)} [K(t) - E(t)], & \eta_{\text{obs}} < \eta_s, \\ \frac{\pi}{2\eta_{\text{obs}}^3}, & \eta_{\text{obs}} = \eta_s, \end{cases} \quad (6)$$

where

$$\eta_{\text{obs}} = \sqrt{(x - x_{\text{obs}})^2 + z^2}, \quad \eta_s = \sqrt{(x - x_s)^2 + z^2}, \quad s = \frac{\sqrt{\eta_{\text{obs}}^2 - \eta_s^2}}{\eta_{\text{obs}}}, \quad t = \frac{\sqrt{\eta_s^2 - \eta_{\text{obs}}^2}}{\eta_s},$$

and E and K are the complete elliptic integrals of the first and the second kind, respectively. We remark that the integral for a kernel in the general case of $y_s \neq y_{\text{obs}}$ can be carried out. However, our experiences have shown that the addition of the corresponding off-line potentials does not improve the final result due to the approximations involved.

The term involving $\mu(x, z)$ in equation (5) can be written as

$$c(x, z) = -\frac{I}{4\pi^2\sigma_0} \frac{\nabla \ln \mu(x, z) \cdot \boldsymbol{\eta}_s}{\eta_s},$$

where $\boldsymbol{\eta}_s = (x - x_s, z)$ is the projection on the x - z plane of the vector from the source to a given subsurface point. Equation (5) can then be written as

$$\varphi_s(x_{\text{obs}}) = \int_{xz} c(x, z) g(x, z; x_s, x_{\text{obs}}) dx dz, \quad (7)$$

where $g(x, z; x_s, x_{\text{obs}}) = \eta_s g_a$ is the new kernel function. The function $c(x, z)$ behaves like a charge density: it is non-zero whenever there is a component of $\boldsymbol{\eta}_s$ parallel to the conductivity gradient $\nabla \ln \mu(\mathbf{r})$. It vanishes identically away from any boundary of the conductivity structure. Thus, if $c(x, z)$ can be properly recovered, the boundary of 2-D subsurface structures would have been located. This leads us to the formulation of charge density imaging.

EQUIVALENT CHARGE DENSITY FORMULATION

Equation (7) is a linear functional relating the equivalent charge density $c(x, z)$ to the secondary potential. As such, secondary potentials recorded at a number of locations x_{obs} , and arising from a fixed source at x_s , can be inverted to recover an estimate of $c(x, z)$. Given that physical charge accumulated at the boundaries between blocks of different conductivities, it follows that an algorithm which is effective in delineating the locations of that charge can generate important information about the structure.

We accomplish this imaging by setting up a linear inverse problem. We first discretize a cross-section of the earth into $m_x \times m_z$ rectangular cells. In each cell $c(x, z)$ is assumed to be constant. Equation (7) becomes

$$\varphi_s^i = \sum_{j=1}^{m_x} \sum_{k=1}^{m_z} A_{jk}^i c_{jk}, \quad i = 1, \dots, n \quad (8)$$

where φ_s^i is the datum at location x_{obs}^i , n is the number of the data available, and A_{jk}^i is the integral of i th kernel function over jk th cell Δ_{jk} ,

$$A_{jk}^i = \int_{\Delta_{jk}} g(x, z; x_s, x_{\text{obs}}^i) dx dz.$$

The number of data is generally far fewer than the number of cells and hence equation (8) is an undetermined system. Equivalently, the solution is non-unique. To obtain a particular solution, we seek a 'simple' charge density which can explain

the observed secondary potential data. Our measure of simplicity is defined by the weighted l_1 norm of the charge density. We do not fit the data exactly but rather introduce a misfit variable ε_i for each data equation and permit a total misfit bounded by a prescribed value. Thus the minimization problem becomes

$$\min \phi = \sum_{j=1}^{m_x} \sum_{k=1}^{m_z} w_{jk} |c_{jk}|, \quad \text{subject to} \quad \sum_{j=1}^{m_x} \sum_{k=1}^{m_z} \frac{A_{jk}^i}{\delta_i} c_{jk} + \varepsilon_i = \frac{\varphi_s^i}{\delta_i}, \quad i = 1, \dots, n, \quad \sum_{i=1}^n |\varepsilon_i| \leq \beta n \sqrt{\frac{2}{\pi}} \quad (9)$$

where δ_i is the estimated standard deviation of the error associated with i th datum, and β is a fit parameter which controls the fit to the data. $n\sqrt{2/\pi}$ is the expected value of the total misfit assuming Gaussian distribution of noise. w_{jk} is a set of weighting coefficients which ultimately determine the type of model which is obtained. We are free to choose any weighting function. We have specified

$$w_{jk} = (z_k - z_0)^{3/2} \eta_s.$$

The first part is introduced to overcome the natural decay of the kernel function with the depth and the second part to compensate the decay of the primary field with the distance. The minimization of the above problem is solved using standard linear programming methods (e.g. Murty 1983). This choice suits our need for finding a sparse representation of the charge density.

When a current is input to the ground the physical charge density depends upon the source position relative to the conductivity anomaly. The charge density c_{ij} found above reflects this relationship. The result of the above inversion only provides with us a partial image of the boundary. However, the field from a different current source position illuminates the boundary in a different way. By inverting for $c(x, z)$ from many different source positions using (7), a relatively complete image of the boundary is obtained.

Taking the advantage of the E-SCAN data set, we can form many sets of common source potential data. Each set can be inverted to yield a part of the boundary image. When all the partial images are combined, they give a rather complete picture. Fig. 2 shows the result obtained by inverting synthetic data generated from a simple prism buried in a uniform half-space. Seven sets of secondary potential data corresponding to different source locations, shown in Fig. 2(a), are used in the inversion. Fig. 2(b) is the combined image. The top and the bottom boundary of the prism are correctly imaged. The pseudo-charge density also has the correct sign. It is negative at the top where the current flows into the conductive body and is positive at the bottom where the current flows out of the prism. Figs 2(c)–(f) show some results from different individual inversions. They clearly show the different parts of the boundary imaged by the potentials from the different source locations.

From the viewpoint of physics, this approach is very appealing. The charge accumulation on the boundary is a physical reality in the DC experiment and any attempt to recover it is valuable. As illustrated in the above example, it has worked satisfactorily for imaging simple structures. However, for a closed body in a uniform half-space, the sum of the charge accumulated on the boundary is zero. So the secondary potential is primarily the field of dipolar and higher order sources. The recovery of the true charge distribution from such fields is difficult and the solution can be highly non-unique.

Because the subsurface charge density depends upon the source position, there is no single distribution of charges which is compatible with all the data. Therefore, in the recovery of the secondary charge density, each inversion uses a single current field. Results from several such individual inversions form a composite image as the final result. A more stable approach would be to invert for a single model using all the data simultaneously. This leads us to the direct formulation to recover a conductivity image.

CONDUCTIVITY FORMULATION FOR 2-D STRUCTURE

Equation (5) presents a linear relationship between the gradients of $\ln \mu(\mathbf{r})$ and the secondary potential. By forming a linear inverse problem to recover $\ln \mu(\mathbf{r})$ directly, we can simultaneously invert data from many different current locations and thereby greatly reduce the non-uniqueness. We adopt the same type of discretization as in the charge imaging. The conductivity section is divided into $m_x \times m_z$ cells each of which is specified by a constant value of $\ln \mu$. The model for the inverse problem then becomes

$$m_{jk} = \ln(\mu_{jk}), \quad j = 1, \dots, m_x, \quad k = 1, \dots, m_z.$$

Under these assumptions, the gradient becomes discrete. $\partial \ln \mu / \partial x$ is non-zero only on the vertical interfaces between cells and $\partial \ln \mu / \partial z$ is non-zero only on the horizontal interfaces,

$$\frac{\partial \ln \mu}{\partial x} = (m_{jk} - m_{j-1,k}) \delta(x - x_j), \quad (x, z) \in \Gamma_{jk}^x, \quad j = 1, \dots, m_x + 1 \quad k = 1, \dots, m_z,$$

$$\frac{\partial \ln \mu}{\partial z} = (m_{jk} - m_{j,k-1}) \delta(z - z_k), \quad (x, z) \in \Gamma_{jk}^z, \quad j = 1, \dots, m_x \quad k = 1, \dots, m_z + 1,$$

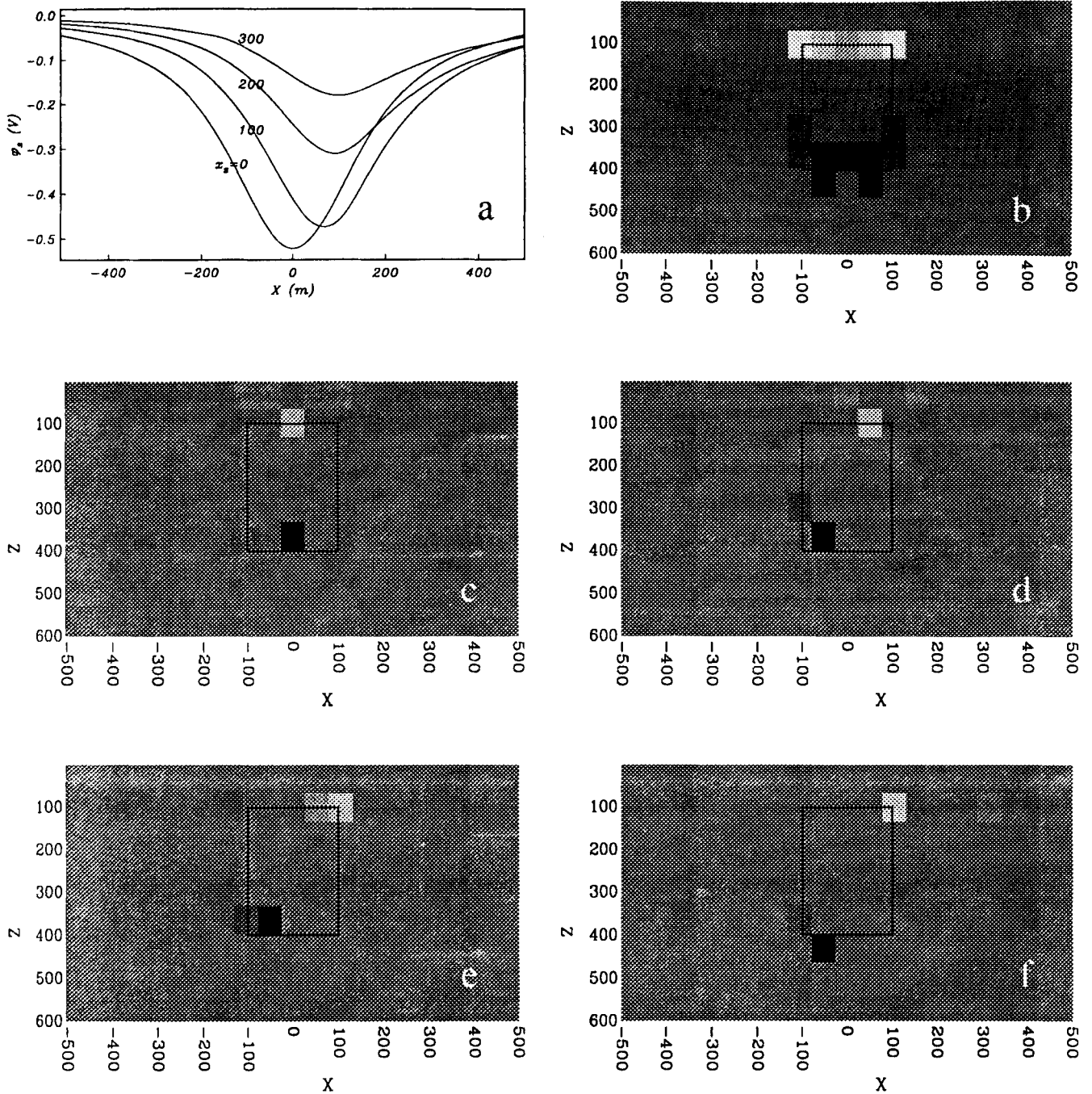


Figure 2. Imaging subsurface structure using charge density. Panel (a) shows the secondary potentials corresponding to the labelled source locations over a 2-D conductive prism buried in a uniform half-space. Panel (b) is the composite of the individually recovered charge density images corresponding to seven sources located from -300 to 300 m in equal spacing. The light region represents the negative charge density and the dark region the positive charge density. The solid line in the image indicates the boundary of the 2-D prism. Panels (c)–(f) are images corresponding to sources at 0 , 100 , 200 , and 300 m, respectively.

where Γ_{jk}^x and Γ_{jk}^z denote the vertical and horizontal interfaces respectively. When the index j equals 0 or $m_x + 1$, or index k equals 0 or $m_x + 1$, the model parameter m_{jk} is taken to be the background value, which is zero.

Substituting the gradient functions into (5) yields a discrete data equation of the form

$$\varphi_s^i = \sum_{j=1}^{m_x} \sum_{k=1}^{m_z} m_{jk} \gamma_{jk}^i, \quad i = 1, \dots, n, \tag{10}$$

where

$$\gamma_{jk}^i = \gamma_{jk}^{xi} - \gamma_{j+1,k}^{xi} + \gamma_{jk}^{zi} - \gamma_{j,k+1}^{zi}, \quad \gamma_{jk}^{xi} = -\frac{I}{4\pi^2\sigma_0} (x_j - x_s^i) \int_{\Gamma_{jk}^x} g_a(x, z; x_s^i, x_{\text{obs}}^i) dz, \quad \gamma_{jk}^{zi} = -\frac{I}{4\pi^2\sigma_0} z_k \int_{\Gamma_{jk}^z} g_a(x, z; x_s^i, x_{\text{obs}}^i) dx.$$

We choose to minimize an objective function composed of a combination of the l_1 norm of the model and the l_1 norm of the gradient.

$$\phi = \alpha \sum_{j,k} w_{jk} |m_{jk}| + (1 - \alpha) \left[\sum_{j,k} w_{jk}^x |m_{jk} - m_{j-1,k}| + \sum_{j,k} w_{jk}^z |m_{jk} - m_{j,k-1}| \right]. \quad (11)$$

The weighting coefficients w_{jk} , w_{jk}^x and w_{jk}^z are introduced to control the relative importance of a particular cell in the objective function based on the cell size and depth. The parameter α takes on a value in $[0, 1]$ and determines the relative importance between model and gradient. Mathematically, the second part is a measure of the variation in the model in the sense of l_1 norm. When α approaches unity, the inversion produces a smallest model without much restriction on the variation. As α approaches zero, the inversion produces a minimum-variation model (Dosso & Oldenburg 1989).

The minimization problem can be solved using standard methods. Variables which can acquire both positive and negative values are replaced by the difference of two positive values. Misfit parameters are also introduced, as they were in the equivalent charge imaging, so that the final data are fit only to within a global tolerance. In addition, an upper and lower bound can also be imposed on the model elements as constraints. The kernel γ_{jk}^i is computed numerically. It can be shown that the kernel γ_{jk}^i is symmetric for interchanging source and receiver locations. Therefore, for every pair of electrodes in the E-SCAN data, only one datum entry is required as the DC potential satisfies the reciprocity.

To illustrate the above algorithms, a set of secondary potential data from a synthetic model is inverted. The model consists of a conductive prism and a resistive prism buried in a uniform half-space (see Fig. 3b). The half-space conductivity is 1 mS m^{-1} . The conductivities of the two prisms are 4 and 0.25 mS m^{-1} , respectively. A set of E-SCAN data is generated over a traverse of 21 grid points. Fig. 3(a) shows the corresponding apparent conductivity pseudo-section. 200 secondary potentials corresponding to this pseudo-section are used in the inversion. The model section is divided into 300 cells with thickness increasing with the depth. An upper bound of 10 for the conductivity contrast is imposed on the solution. Fig. 3(c) shows the result of a minimum variation type model with $\alpha = 0.9$. The conductive prism is defined reasonably well. So is the top of the resistive prism. The poorer recovery of the bottom of the resistive prism is due to the fact that the Born approximation differs more from the true potential in the case of resistive prisms. However, for the purpose of imaging the structure, the algorithm has worked satisfactorily.

APPROXIMATE 3-D INVERSION

In principle, the techniques used in 2-D analyses can be extended to 3-D conductivities. In practice however, the large number of model elements and data result in a large matrix to be inverted and this makes the approaches impractical. We choose to develop a different methodology motivated by the existence of E-SCAN data.

Applying the vector identity $\nabla \cdot (\psi \mathbf{a}) = \psi \nabla \cdot \mathbf{a} + \nabla \psi \cdot \mathbf{a}$, for an arbitrary scalar ψ and an arbitrary vector \mathbf{a} , to the integrand in (4) yields

$$\varphi_s(\mathbf{r}_{\text{obs}}) = \frac{I}{4\pi^2\sigma_0} \int_V \ln \mu(\mathbf{r}) \nabla \cdot \left(\frac{1}{|\mathbf{r} - \mathbf{r}_{\text{obs}}|} \nabla \frac{1}{|\mathbf{r} - \mathbf{r}_s|} \right) dv + \frac{1}{4\pi^2\sigma_0} \int_V \nabla \cdot \left(\ln \mu(\mathbf{r}) \frac{1}{|\mathbf{r} - \mathbf{r}_{\text{obs}}|} \nabla \frac{1}{|\mathbf{r} - \mathbf{r}_s|} \right) dv. \quad (12)$$

With the aid of Gauss's theorem the last integral in the above equation can be expressed as

$$\beta = \frac{1}{4\pi^2\sigma_0} \int_S \ln \mu(\mathbf{r}) \frac{1}{|\mathbf{r} - \mathbf{r}_{\text{obs}}|} \nabla \frac{1}{|\mathbf{r} - \mathbf{r}_s|} \cdot \hat{\mathbf{n}} ds,$$

where S represents the entire boundary of the lower half-space with outward normal vector $\hat{\mathbf{n}}$. The contribution to β from the flat upper surface of the half-space is zero because

$$\nabla \frac{1}{|\mathbf{r} - \mathbf{r}_s|} \cdot \hat{\mathbf{n}} = 0$$

there. Along the remaining boundaries,

$$\frac{1}{|\mathbf{r} - \mathbf{r}_{\text{obs}}|} \nabla \frac{1}{|\mathbf{r} - \mathbf{r}_s|} \cdot \hat{\mathbf{n}} \propto \frac{1}{|\mathbf{r}|^3} \quad \text{as } |\mathbf{r}| \rightarrow \infty,$$

and hence the boundary integral vanishes there. Thus β is identically zero.

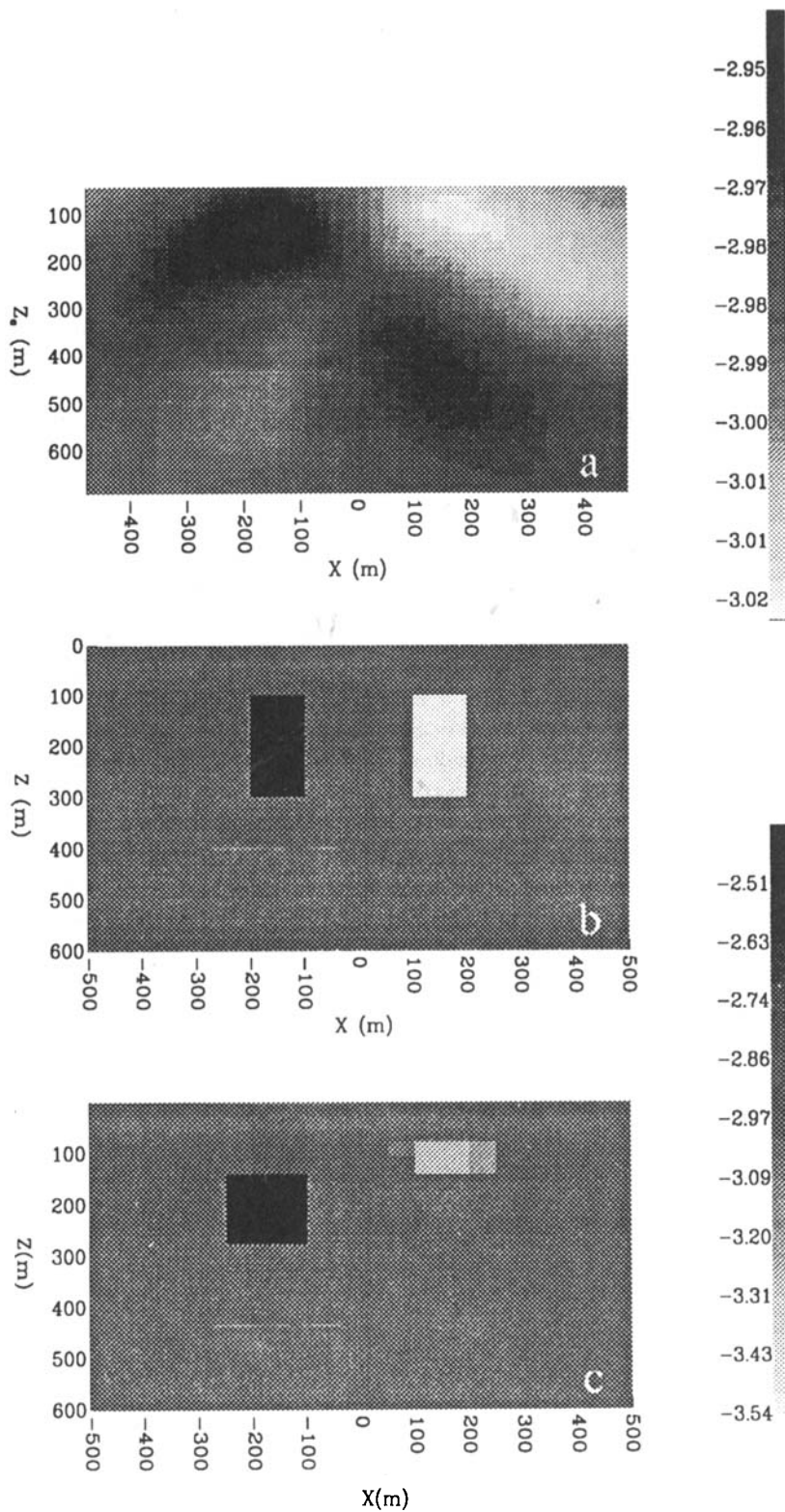


Figure 3. Imaging subsurface conductivity. The synthetic model shown in panel (b) consists of a conductive (4 mS m^{-1}) and a resistive 2-D prism (0.25 mS m^{-1}) in a uniform half-space of 1 mS m^{-1} . 200 secondary potential data on the surface are used in the inversion. Panel (a) is the corresponding apparent conductivity pseudo-section. Panel (c) is the recovered conductivity model. The upper grey scale is for panel (a) and the lower grey scale is for panels (b) and (c). The scale is in $\log_{10} \sigma$.

Applying the same vector identity to the first integral in (12) yields

$$\varphi_s(\mathbf{r}_{\text{obs}}) = -\frac{l}{4\pi^2\sigma_0} \int_V \ln \mu(\mathbf{r}) \nabla \frac{1}{|\mathbf{r} - \mathbf{r}_{\text{obs}}|} \cdot \nabla \frac{1}{|\mathbf{r} - \mathbf{r}_s|} dv + \frac{l}{4\pi^2\sigma_0} \int_V \ln \mu(\mathbf{r}) \frac{1}{|\mathbf{r} - \mathbf{r}_{\text{obs}}|} \nabla^2 \frac{1}{|\mathbf{r} - \mathbf{r}_s|} dv. \quad (13)$$

The second term in (13) vanishes identically since

$$\nabla^2 \frac{1}{|\mathbf{r} - \mathbf{r}_s|} = -4\pi\delta(\mathbf{r} - \mathbf{r}_s)$$

and $\ln \mu(\mathbf{r}_s) = 0$ because it has been assumed that the surface conductivity is σ_0 . Thus we obtain the following expression for the secondary potential on the surface:

$$\varphi_s(\mathbf{r}_{\text{obs}}) = -\frac{l}{4\pi^2\sigma_0} \int_V \ln \mu(\mathbf{r}) \nabla \frac{1}{|\mathbf{r} - \mathbf{r}_s|} \cdot \nabla \frac{1}{|\mathbf{r} - \mathbf{r}_{\text{obs}}|} dv. \quad (14)$$

Equation (14) is a Fredholm equation of the first kind relating the secondary potential to the perturbation of logarithmic conductivity. The equation is similar to that presented by Boerner & West (1989) which was derived using an integral equation for the potential on the boundary of an isolated inhomogeneity with constant conductivity.

E-SCAN data are generally acquired in a regular grid. As such, it is convenient to explicitly consider data generated from pole-pole arrays with fixed separations and orientations. As in Fig. 4, let \mathbf{r}_0 be the mid-point of the array, and let $2\mathbf{l}$ be the vector pointing from source electrode to potential electrode. Then

$$\mathbf{r}_s = \mathbf{r}_0 - \mathbf{l}, \quad \mathbf{r}_{\text{obs}} = \mathbf{r}_0 + \mathbf{l}.$$

Substituting into (14) and transforming to apparent resistivities yields

$$\rho_a(\mathbf{r}_0; \mathbf{l}) = \rho_0 - \frac{\rho_0 l}{\pi} \int_V \ln \mu(\mathbf{r}) \nabla \frac{1}{|\mathbf{r}_0 + \mathbf{l} - \mathbf{r}|} \cdot \nabla \frac{1}{|\mathbf{r}_0 - \mathbf{l} - \mathbf{r}|} dv, \quad (15)$$

where $l = |\mathbf{l}|$. Noticing that $\mathbf{r}_0 = (x, y, 0)$ and $\mathbf{l} = (l_x, l_y, 0)$, we recognize that equation (15) involves a convolution operation in the x - y domain. Thus the surface pole-pole apparent resistivity can be expressed as

$$\rho_a(\mathbf{r}_0; \mathbf{l}) = \rho_0 + \rho_0 \int_0^\infty \ln \mu(\mathbf{r}) \otimes \otimes g(\mathbf{r}; \mathbf{l}) dz, \quad (16)$$

where $\rho_0 = 1/\sigma_0$, the symbol $\otimes \otimes$ denotes the 2-D convolution operation and $g(\mathbf{r}, \mathbf{l})$ is the kernel function

$$g(\mathbf{r}; \mathbf{l}) = -\frac{l}{\pi} \nabla \frac{1}{|\mathbf{r} + \mathbf{l}|} \cdot \nabla \frac{1}{|\mathbf{r} - \mathbf{l}|} = -\frac{l[(x+l_x)(x-l_x) + (y+l_y)(y-l_y) + z^2]}{\pi[(x+l_x)^2 + (y+l_y)^2 + z^2]^{3/2}[(x-l_x)^2 + (y-l_y)^2 + z^2]^{3/2}}. \quad (17)$$

Equation (16) relates the surface pole-pole apparent resistivity data from a fixed array configuration to the subsurface conductivity structure. It is noticed that the anomalous part of the apparent resistivity is a depth integral of the conductivity perturbation convolved with a kernel in the x - y domain.

Define the Fourier transform over the infinite plane and its inverse transform as (Bracewell 1978)

$$\mathcal{F}_{xy}[f(x, y)] = \int_{-\infty}^{\infty} \int_{-\infty}^{\infty} f(x, y) e^{-ipx - iqy} dx dy, \quad \mathcal{F}_{xy}^{-1}[\bar{f}(p, q)] = \frac{1}{4\pi^2} \int_{-\infty}^{\infty} \int_{-\infty}^{\infty} \bar{f}(p, q) e^{ipx + iqy} dp dq.$$

Taking the 2-D Fourier transform of equation (16) and applying the convolution theorem yields

$$\bar{e}_j(p, q) = \int_0^\infty \bar{m}(p, q, z) \bar{g}_j(p, q, z) dz, \quad j = 1, \dots, n_l, \quad (18)$$

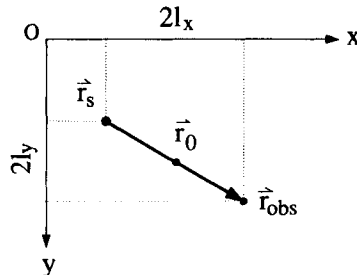


Figure 4. Geometry of the surface pole-pole array is specified by a vector $2\mathbf{l}$ pointing from the source location \mathbf{r}_s to observation \mathbf{r}_{obs} . \mathbf{r}_0 is the mid-point of the array, where the apparent resistivity is recorded.

where (p, q) are transform variables representing the wavenumber in x - and y -directions and

$$\bar{e}_j(p, q) = \mathcal{F}_{xy}[\rho_a(\mathbf{r}_0; \mathbf{l}_j)/\rho_0 - 1], \quad j = 1, n_l, \quad \bar{m}(p, q, z) = \mathcal{F}_{xy}[\ln \mu(\mathbf{r})], \quad \bar{g}_j(p, q, z) = \mathcal{F}_{xy}[g(\mathbf{r}; \mathbf{l}_j)], \quad j = 1, n_l.$$

The index j identifies the j th pole–pole array. In an E-SCAN data set, many different pole–pole arrays exist; each is specified by a unique separation and orientation of the current and potential electrodes. We denote the number of distinct pole–pole arrays by n_l .

Equation (18) is a Fredholm integral equation of the first kind. The data $\bar{e}_j(p, q)$ and model $\bar{m}(p, q, z)$ are complex because they are the Fourier transforms of arbitrary real functions. The kernels, however, are real. This results because of the symmetry of (17) about the origin. At each wavenumber, equation (18) shows that there are n_l constraints upon the model $\bar{m}(p, q, z)$. Linear inverse theory can therefore be used to recover $\bar{m}(p, q, z)$ as a function of the depth z (Backus & Gilbert 1967; Oldenburg 1984). Completing this inversion at all wavenumbers yields the model $\bar{m}(p, q, z)$. The 3-D spatial distribution of the conductivity is obtained by performing an inverse 2-D Fourier transform in the horizontal directions at sampled depths.

The implementation of the above inversion method requires that a background conductivity be estimated, that pole–pole apparent resistivity data maps corresponding to different separations and directions are gathered and interpolated to a common grid so they can be Fourier transformed, that kernel functions are evaluated, and 1-D inversion problems are solved. We consider these aspects next.

Data

The data required for the 1-D inversions are generated by applying a 2-D spatial Fourier transform to the quantity $(\rho_a - \rho_0)/\rho_0$ for each electrode configuration. This requires a reliable estimate of the background resistivity ρ_0 . Experiments with both synthetic and field data sets show that the mean value of the apparent resistivity data, i.e., the best fitting half-space model, provides such an estimate. It works well especially for structures with localized inhomogeneities or where the conductivity is distributed about a regional value.

This process also requires that the initial E-SCAN field data be interpolated and extrapolated. The procedure is best explained by using Fig. 5. An E-SCAN survey is generally carried out over a regular grid. A basic grid is shown by the solid lines in Fig. 5. Each node in that grid would have been occupied by a current or potential electrode as the survey data are collected. Suppose that a data map is desired for $\bar{l}_j = (\Delta x/2, \Delta y)$. This pole–pole configuration is given by the arrows in Fig. 5. The apparent resistivity for each electrode pair having this orientation can be evaluated and assigned to the mid-point between these two electrodes. The solid dots indicate the locations at which apparent resistivities can be evaluated for this particular electrode pair. Notice that this area activated by the solid dots is smaller than the initial survey area. The size of the activated area decreases as $|\bar{l}_j|$ increases.

We have not yet specified a domain on which the inversion is to be carried out. We now select the x - y limits of the domain to be a rectangle which is larger than the initial survey area and contains the initial survey at its centre. Typically, as illustrated in Fig. 5, the distance between the survey grid and the boundaries of the inversion domain have been set equal to the maximum values of l_x and l_y in the x - and y -directions respectively.

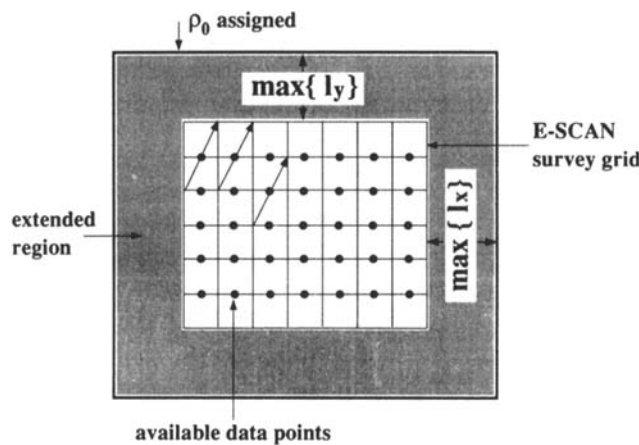


Figure 5. Specification of the data map. The intersections of solid lines indicate the E-SCAN grid points. The potential data are acquired over all grid points but the pole–pole apparent resistivity is defined only in a smaller area. One possible array configuration is shown by the arrows in the diagram, which point from the source to the potential location. The apparent resistivity data for this array can be formed only on the locations indicated by solid dots. This activated area is smaller than the survey area and decreases as $|\bar{l}_j|$ increases. To generate a data map suitable for inversion, a mathematical area is defined by extending the original E-SCAN survey region half of the maximum array separation in x - and y -directions.

The remaining step is to define a rectangular grid on the surface of the inversion model domain. Because some data maps (for example that shown in Fig. 5) yield data at locations mid-way between the nodes of the survey grid, it is reasonable to select a spatial discretization for the Fourier transform grid which is half of the field survey grid spacing. We generally use this. With this choice of gridding there will be many points on the inversion grid that are not defined directly by values from the survey grid. Both interpolation and extrapolation are required. Interpolation inside an activated area (e.g. within the rectangle generated by the solid dots in Fig. 5) is not difficult but extrapolation is always dangerous. In order to avoid the introduction of extraneous artifacts and also ensure that the data to be Fourier transformed are zero around the edges, we specify the apparent resistivity around the boundary of the inversion grid to be ρ_0 , the background resistivity. The evaluation of apparent resistivities at all nodes on the inversion grid can now be obtained by interpolating a data set consisting of the interior activated points and the outside boundary points. We apply an interpolator consisting of a combination of Laplacian and cubic spline components to $\ln \rho_a$. After interpolation, the percentage anomaly $(\rho_a - \rho_0)/\rho_0$ is calculated and Fourier transformed to generate the data actually used in the inversion.

Kernel function

Equation (17) gives the expression for the kernel function in the spatial domain. For illustration, Fig. 6 shows three slices through the spatial kernel function, $g(\mathbf{r}; \mathbf{l})$, for a given \mathbf{l} . The distance between the electrodes is 50 m and the depth slices are at $z = 1, 20$, and 40 m respectively. At shallow depths the character of the kernel function is dominated by two large dipole-like features which are directly beneath the current and potential electrodes. These features become singularities as $z \rightarrow 0$. At greater depths these peaks become smoother and spread out horizontally. We note, however, that for shallow depths, (e.g. $z = 1$ and 20 m in Fig. 6) the spatial kernel function has an inner region of opposite sign. These observations are all in agreement with our understanding of the pole-pole DC resistivity experiment. For a given separation, the array is sensitive to smaller changes in the conductivity structure from a shallow region but it responds only to a broader average of conductivity structure at deeper regions. The positive region agrees with the fact that the array has a negative response to relatively shallow anomalies, for instance, it measures a resistive anomaly over a shallow conductor (e.g. Li & Oldenburg 1991).

The kernels $\bar{g}(p, q, z)$ needed in the 1-D inversion require that (17) be spatially Fourier transformed. We have not been able to obtain an analytic solution and therefore have calculated these numerically. Our approach is to evaluate each 3-D kernel at a specified set of depths (z_1, \dots, z_n) and then Fourier transform each depth slice. The results are combined to yield a discretized kernel $\bar{g}(p, q, z_k)$ ($k = 1, n_l$). This discrete representation is interpolated to provide a continuous representation of each kernel.

The spatial Fourier transforms of the slices shown in Fig. 6 are given in Fig. 7. The Fourier transform at shallow depth is characterized by numerous oscillations and large bandwidth. For greater depths, the transforms die out more rapidly with increasing wavenumber. At any wavenumber, these plots provide three point evaluations of $\bar{g}(p, q, z)$. The complete kernels $\bar{g}_j(p, q, z)$ corresponding to $(p, q) = (0.012, 0)$ are shown in Fig. 8. Kernel functions corresponding to small $|l_j|$ have more structure and amplitude toward the surface than do those pertaining to larger offsets. Kernel functions for large source-receiver separation decay more slowly with depth. This complies with the fact that a larger separation array has a greater depth of penetration. We note also that the kernels are smooth functions of depth. Since the array separations are increasing linearly, the kernels for large offsets become similar. Effectively there is little new information provided by kernel-8 that is not already in kernel-7. That is, the kernels associated with the two largest offsets are almost linearly dependent for this particular choice of (p, q) . The smoothness and lack of structure exhibited by the kernels also adds insight into the nature of the inversion results. We would not expect for example that these kernels could provide any vertical resolution about the conductivity below depths of about 200 m.

For a fixed array separation, the dominating portion of the kernel function shifts towards the surface as the wavenumber increases. We can characterize this by the median depth of the absolute area under the kernel function. At zero wavenumber this median depth is in fact the effective depth of pole-pole array defined by Edwards (1977). The decrease of this depth with the increase of wavenumber indicates that Edwards' effective depth sets an upper bound on the depth of investigation. It becomes smaller as the lateral resolution requirement increases. For the same reason, the recovered conductivity model becomes smoother as depth increases.

Inversion

With the data and kernel functions evaluated in the wavenumber domain, we now turn attention to the solution of the inverse problem. According to (18), at each wavenumber (p, q) we need to invert a Fredholm equation of the first kind to recover a complex model $\bar{m}(p, q, z)$. There exists an infinite number of models which adequately reproduce the n_l complex and inaccurate data e_j ($j = 1, n_l$). Our inversion will be formulated to generate a model with 'minimum' structure with respect to the background conductivity.

The mathematical development of the approximate 3-D inversion made use of the Born approximation. That

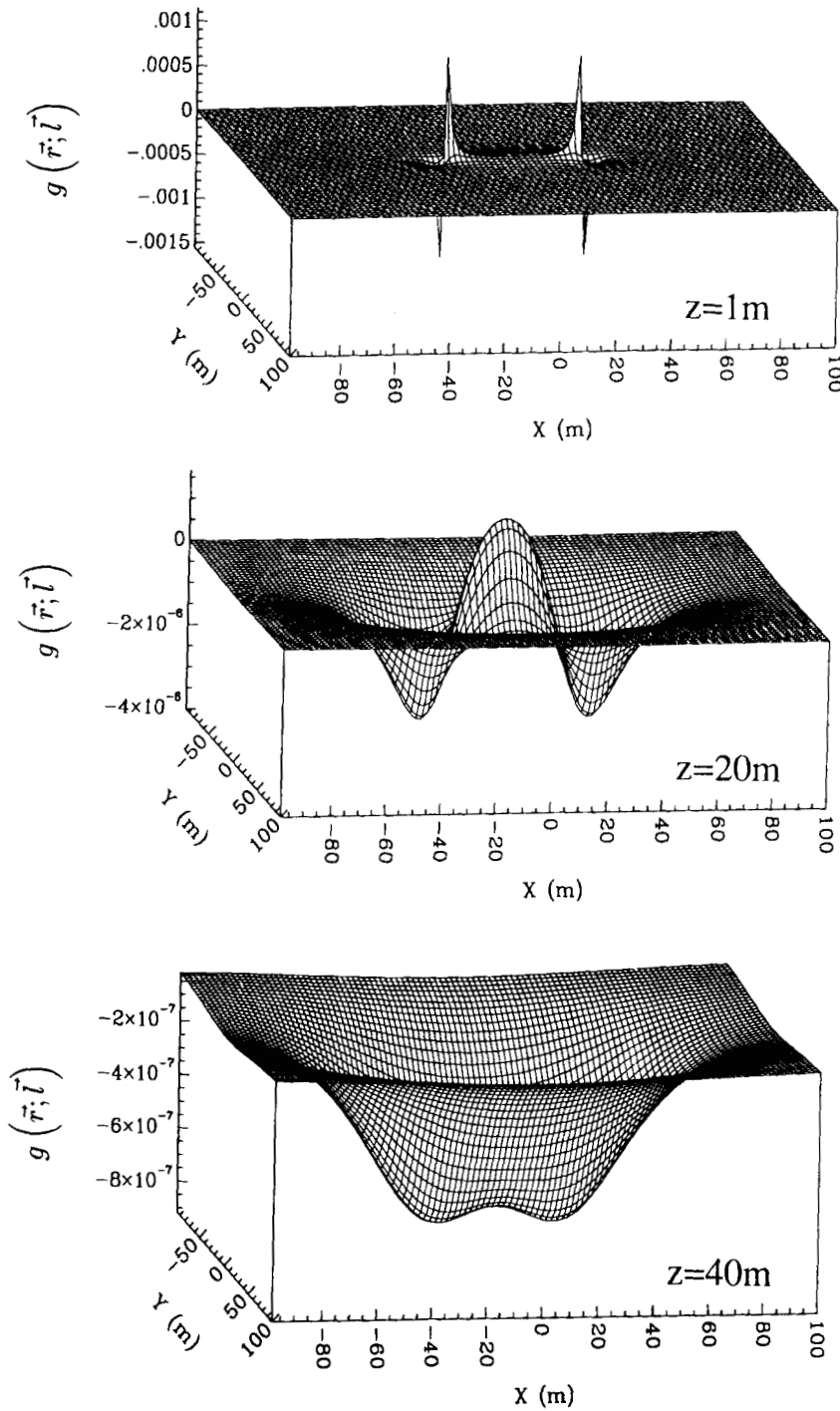


Figure 6. Spatial domain kernel function corresponding to $(l_x, l_y) = (25, 0)$ at depths $z = 1, 20, 40$ m respectively.

approximation is valid when the conductivity differs only slightly from the half-space value. For consistency, it is therefore reasonable to compute a conductivity model which deviates as little as possible from this background model. We construct such a 3-D conductivity model by finding perturbations to a base model defined by the estimated half-space conductivity σ_0 , the reciprocal of ρ_0 used in the data reduction. We therefore seek a model which minimizes

$$\phi(\mu) = \int_x \int_y \int_z w(z) [\ln \mu(\vec{r})]^2 dx dy dz \tag{19}$$

where $w(z)$ is an arbitrary positive weighting function. Using Parseval's theorem, (19) can be written as

$$\phi(\mu) = \sum_p \sum_q \int_z w(z) |\bar{m}(p, q, z)|^2 dz. \tag{20}$$

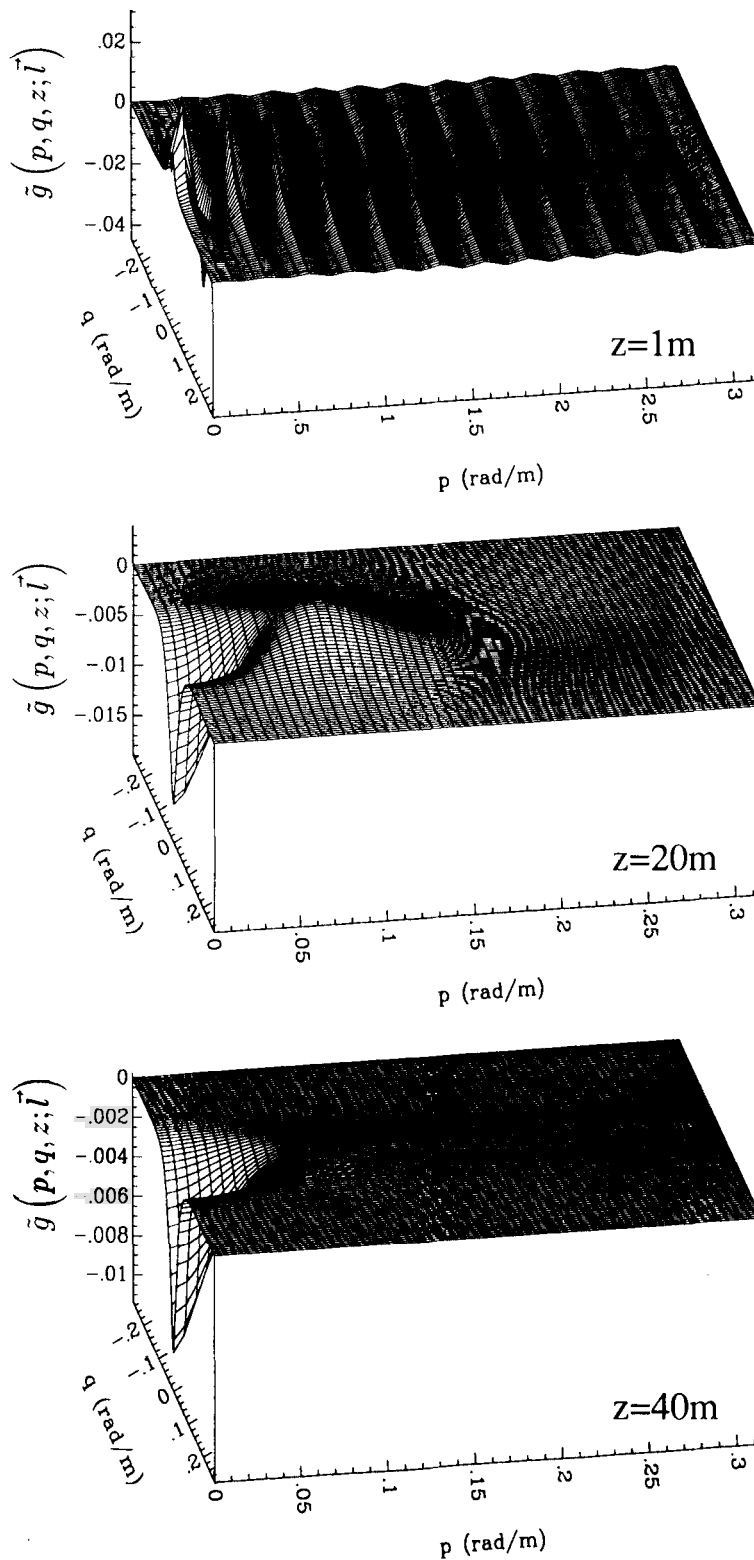


Figure 7. Wavenumber domain kernel function corresponding to $\mathbf{l} = (25, 0)$ at the depth of 1, 20, and 40 m. These three slices are the 2-D Fourier transforms of the spatial kernels in Fig. 6. They provide three point evaluations on the kernel corresponding to the given \mathbf{l} used in the 1-D inversion at all wavenumbers. The complete kernel is obtained by evaluating all depth slices.

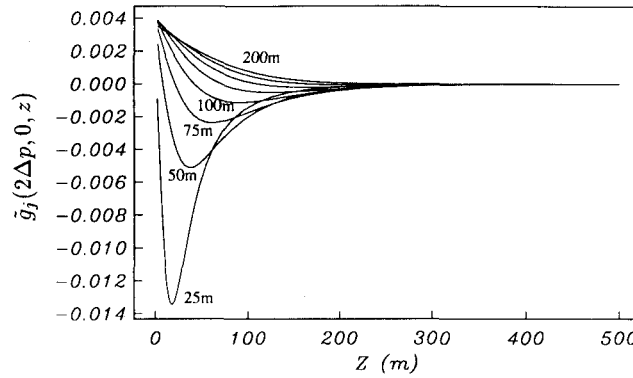


Figure 8. A set of kernels at wavenumber $(p, q) = (0.012, 0)$ for arrays in the x -direction, i.e., $\mathbf{l} = (l_x, 0)$. The curves correspond to arrays with l_x ranging from 25 to 200 m in equal increments of 25 m.

In this form, we observe that the total objective function is a sum of positive quantities. The objective function is effectively decoupled and the total objective function is minimized by minimizing the integral of the square of $\bar{m}(p, q, z)$ at each wavenumber. We are now in a position to specify the 1-D inversion.

At each wavenumber our data equations (18) have the form

$$\bar{e}_j = \int_0^\infty \bar{m}(p, q, z) \bar{g}_j(p, q, z) dz, \quad j = 1, \dots, n_l,$$

where \bar{e}_j and $\bar{m}(p, q, z)$ are complex and $\bar{g}_j(p, q, z)$ are real. The model and kernels are assumed to reside in a Hilbert space \mathcal{M} of complex functions defined on the region $(0, z_{\max})$ where z_{\max} is some maximum depth of interest and is sufficiently great so that all kernel functions have negligible amplitude by that depth. If \bar{g} and \bar{h} are any two functions in \mathcal{M} , then their inner product is given by

$$(\bar{g}, \bar{h}) = \int_0^{z_{\max}} w(z) \bar{g}(z) \bar{h}^*(z) dz \tag{21}$$

where the $*$ denotes complex conjugate. The norm on \mathcal{M} is defined by

$$\|\bar{m}\| = \left(\int_0^{z_{\max}} w(z) |\bar{m}(z)|^2 dz \right)^{1/2}. \tag{22}$$

The data provide only n_l constraints upon the model and hence $\bar{m}(p, q, z)$ cannot be obtained unambiguously from them. There are, in fact, infinitely many models which fit the data exactly (e.g. Backus & Gilbert 1967). Given that the data are also inaccurate, we choose to find that particular model which minimizes

$$\phi(\bar{m}) = \|\bar{m}\|^2 + \theta^{-1} \sum_j |\bar{e}_j - (\bar{m}, \bar{g}_j^w)|^2 \tag{23}$$

where θ is a Lagrange multiplier and $\bar{g}_j^w(z) = \bar{g}_j(z)/w(z)$. The minimization is straightforward. Any function $\bar{m} \in \mathcal{M}$ can be written as $\bar{m} = \bar{m}^{\parallel} + \bar{m}^{\perp}$ where $\bar{m} \in \mathcal{M}^{\parallel} = \text{asp} \{ \bar{g}_j^w \}$ and \mathcal{M}^{\perp} is the complement of \mathcal{M}^{\parallel} . It is clear that \bar{m}^{\perp} does not contribute to the data misfit but it will contribute to the model norm. As such, a minimization of $\phi(\bar{m})$ demands that

$$\bar{m}(p, q, z) = \sum_{j=1}^n \alpha_j \bar{g}_j^w(p, q, z) \tag{24}$$

where α_j are coefficients to be determined. Substituting into (23) and writing the objective function in a matrix/vector notation yields

$$\phi(\bar{m}) = \mathbf{\alpha}^H \mathbf{\Gamma} \mathbf{\alpha} + \theta^{-1} (\mathbf{e} - \mathbf{\Gamma} \mathbf{\alpha})^H (\mathbf{e} - \mathbf{\Gamma} \mathbf{\alpha}) \tag{25}$$

where H denotes complex conjugate transpose and $\mathbf{\Gamma}$ is a real symmetric positive definite inner product matrix with elements

$$\Gamma_{ij} = \int_0^{z_{\max}} w(z) \bar{g}_i^w(p, q, z) \bar{g}_j^w(p, q, z) dz$$

and $\mathbf{\alpha} = (\alpha_1, \dots, \alpha_n)^T$, $\mathbf{e} = (\bar{e}_1, \dots, \bar{e}_{n_l})^T$. Perturbing the coefficient $\mathbf{\alpha}$ in equation (25) and using a variational principle to carry out the minimization yields

$$\mathbf{\Gamma} \mathbf{\alpha} - \theta^{-1} \mathbf{\Gamma}^H (\mathbf{e} - \mathbf{\Gamma} \mathbf{\alpha}) = 0.$$

Since $\mathbf{\Gamma}$ is positive definite and symmetric this may be written as

$$(\mathbf{\Gamma} + \theta \mathbf{I})\boldsymbol{\alpha} = \mathbf{e}. \quad (26)$$

The solution of (26) is most easily obtained by writing $\mathbf{\Gamma} = \mathbf{R}\mathbf{\Lambda}\mathbf{R}^T$, where $\mathbf{\Lambda}$ is a diagonal matrix containing the eigenvalues in descending order, $\mathbf{\Lambda} = \text{diag}(\lambda_1, \dots, \lambda_n)$, and \mathbf{R} is a unitary matrix composed of corresponding eigenvectors $\mathbf{R} = (\mathbf{r}_1, \dots, \mathbf{r}_n)$. The solution of (26) is then given by

$$\boldsymbol{\alpha} = \mathbf{R}(\mathbf{\Lambda} + \theta \mathbf{I})^{-1}\mathbf{R}^T\mathbf{e}. \quad (27)$$

The major difficulty in carrying out the inversion is specifying the value of θ for each 1-D inversion. If the data errors were Gaussian, independent with zero mean and known standard deviation there would be no problem. The procedure would be to first normalize each data equation by the standard deviation of the datum and then adjust θ until a desired misfit value is reached. A desired misfit might be $\mathcal{E}[\chi^2] \approx n_r$.

The errors in our inversion do not comply with the simple Gaussian assumption. In addition to measurement errors on the initial potential data, we have several other major sources of errors. Errors are introduced into the data by the extrapolation of the known data to fill the mathematical area in which the inversion is carried out; errors exist in the model representation associated with the 1-D Fredholm equation which is inexact due to the Born approximation; errors are introduced into both data and model by incorrect estimation of the background conductivity σ_0 . Therefore, our data are biased and non-Gaussian in realistic problems. Nevertheless, we have attempted to incorporate a Gaussian type strategy as much as possible.

Our approach has been to first estimate an approximate error for each datum. These will be interpreted either as approximate standard deviations or at least used as a relative weighting for the different data to be inverted. The estimation of the errors are obtained in the following manner. The errors on initial apparent resistivity data in each map are converted to the variance of wavenumber domain datum $\tilde{e}_j(p, q)$. Since the initial data errors are assumed Gaussian, zero mean and uncorrelated and the Fourier transform kernel has a unit amplitude, this variance is equal to the sum of the variance of the initial error. This error is then scaled by the ratio of the total area to activated area. In the estimation of the initial error, an upper and lower bound on the possible error are imposed. The lower bound is especially useful for those data with small magnitude.

We have used the above errors in three ways. In the first we have accepted these values as valid standard deviations, normalized the data equations by these standard deviations and chosen θ so that the chi-squared misfit was equal to n_r .

In the second method we use the estimated standard deviations as relative weightings for the data equations but chose θ in accordance with its effect on the model norm. The model norm increases monotonically as θ decreases and is easily evaluated in the spectral domain. Using the decomposition of $\mathbf{\Gamma}$, we can define a set of rotated basis function (Parker 1977),

$$\psi_i(z) = \sum_{j=1}^n r_{ji} \tilde{g}_j^w(p, q, z), \quad (28)$$

where r_{ji} is the j th element of eigenvector \mathbf{r}_i . $\psi_i(z)$'s form an orthogonal set, i.e.,

$$(\psi_i, \psi_j) = \lambda_i \delta_{ij}, \quad (29)$$

where δ_{ij} is the Kronecker delta. Then the regularized solution is given by

$$\tilde{m}(p, q, z) = \sum_{i=1}^n \frac{\hat{e}_i}{\lambda_i + \theta} \psi_i(z), \quad (30)$$

where \hat{e}_i is the i th element of the rotated data vector $\hat{\mathbf{e}} = \mathbf{R}^T\mathbf{e}$. It follows from the orthogonality of $\psi_i(z)$'s that

$$\|\tilde{m}\|^2 = \sum_{i=1}^n \lambda_i \left(\frac{\hat{e}_i}{\lambda_i + \theta} \right)^2. \quad (31)$$

The curve $\|\tilde{m}\|^2(\theta)$ is usually smooth and often characterized by a near-vertical slope for small θ , near-zero slope for large θ . The value of θ corresponding to the onset of rapid norm increase, or the value of θ where the tangent to the curve has a given slope k (e.g. $k = -1.0$) can serve as estimates for θ used in the inversion. Without referring to the data misfit, this approach is somewhat arbitrary in the choice of the slope k within this permissible small range. Therefore, when choosing θ based upon a slope criterion, the value of the slope k is best chosen by incorporating a global misfit as done in conjunction with using a single value for θ as presented next.

Our third approach is an attempt to find a single value of θ that is used to regularize all 1-D inversions. A given value of θ will generate a model from which predicted Born data can be calculated. The total chi-squared misfit, evaluated only for the original field data is given by

$$\chi^2 = \sum_{j=1}^{n_1} \left(\frac{\rho_{aj}^o - \rho_{aj}^p}{\delta_j} \right)^2, \quad (32)$$

where ρ_{aj}^o and ρ_{aj}^p are observed and predicted apparent resistivity values, respectively, δ_j is the estimated error of each datum and n_t is the total number of the apparent resistivity data used in the inversion, which are available directly from the initial survey. It should be noted that this χ^2 is the misfit for the approximate equation, it is not a true misfit. Carrying out the inversion for a number of values of θ yields a curve $\chi^2(\theta)$ which can be interrogated to estimate an optimum value or to find that θ which corresponds to an expected χ^2 . This approach has the advantage that the regularization is controlled exactly by misfit to the original data. It does require that the inversion be carried out a number of times but that poses no computational difficulties. The CPU time needed for all 1-D inversions is only a small fraction of that used for computing the kernel functions. Once the kernels are computed, they can be stored and additional inversions can be carried out efficiently.

Synthetic examples show that the first and third approaches tend to over-damp the solution at higher wavenumbers and the resulting model is dominated by a few low wavenumber components. The second method avoids this problem and produces a better model. We generally use this approach.

Table 1. Parameters of the five-prism model.

Prism	x-dimension (m)	y-dimension (m)	z-dimension (m)	Conductivity (mS/m)
S1	225–325	225–325	0–40	10.0
S2	275–675	375–475	0–40	5.0
S3	325–675	626–675	0–40	0.5
B1	275–625	275–375	50–250	0.5
B2	375–475	475–675	75–275	10.0

Examples

To illustrate the algorithm, we present the inversion results for a synthetic and a field data set. The synthetic data set is generated over a 21×21 grid of 50 m spacing for a model consisting of five prisms buried in a uniform half-space. Table 1 lists the model parameters. The perspective view of the model layout is shown in Fig. 9. Prisms B1 and B2 are the buried targets. Prisms S1, S2, and S3 simulate near surface variations in the conductivity. The apparent resistivity maps in both x - and y -directions with separations ranging from 1 to 8 grid spacings and in xy - and yx -diagonal directions with separations from 1 to 5 grid spacings are gathered. A total of 26 data maps are used in the inversion (i.e., there are 26 complex data for each 1-D inversion in the wavenumber domain). No *a priori* information except the background conductivity is given. Fig. 10 is the comparison of the true and recovered model in a section at $x = 450$ m which cuts through the four major prisms. Figs 11 and 12 show the comparison at two different depths. Geometrically, the definition of the surface prisms is excellent. The image becomes less sharp as the depth increases. The magnitude of the recovered anomaly decreases with the depth. In general, the conductivity of the surface blocks is overestimated while that of the deeper ones is underestimated. Because of the loss of resolution and magnitude at the depth, the bottom of the buried prisms is poorly defined. Instead, there is a smooth transition from the anomaly to the background. The loss of resolution is due to the limited bandwidth of the data and the fact that the kernel function in the wavenumber domain decays more rapidly with depth at higher wavenumbers. The loss of amplitude is due to the nature of smallest model construction, where a ridge regression parameter is used to regularize the solution. Overall the recovered model appears as a depth varying filtered version of the true model. All anomalies are well resolved. Despite the influence of the surface conductivity variations, the buried prisms are clearly defined.

It is noteworthy that three conductivity blocks with high contrasts extend to the surface. This is apparently in violation of

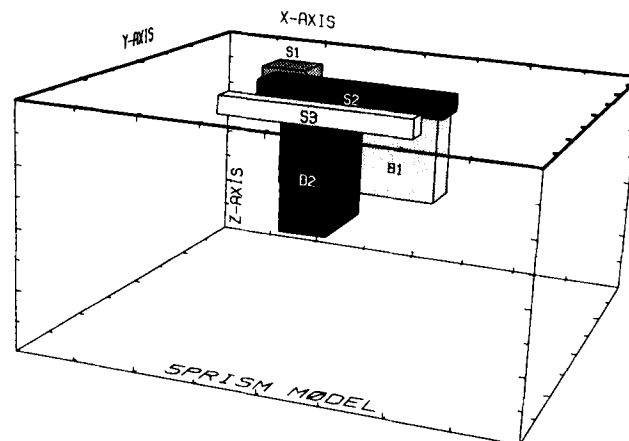


Figure 9. The perspective view of the synthetic model consisting of five prisms embedded in a uniform half-space of 1.0 mS m^{-1} . The surface prisms S1 (5.0 mS m^{-1}), S2 (10.0 mS m^{-1}) and S3 (0.5 mS m^{-1}) simulate the near surface variations in the conductivity. The B1 (0.5 mS m^{-1}) and B2 (10.0 mS m^{-1}) are the buried targets.

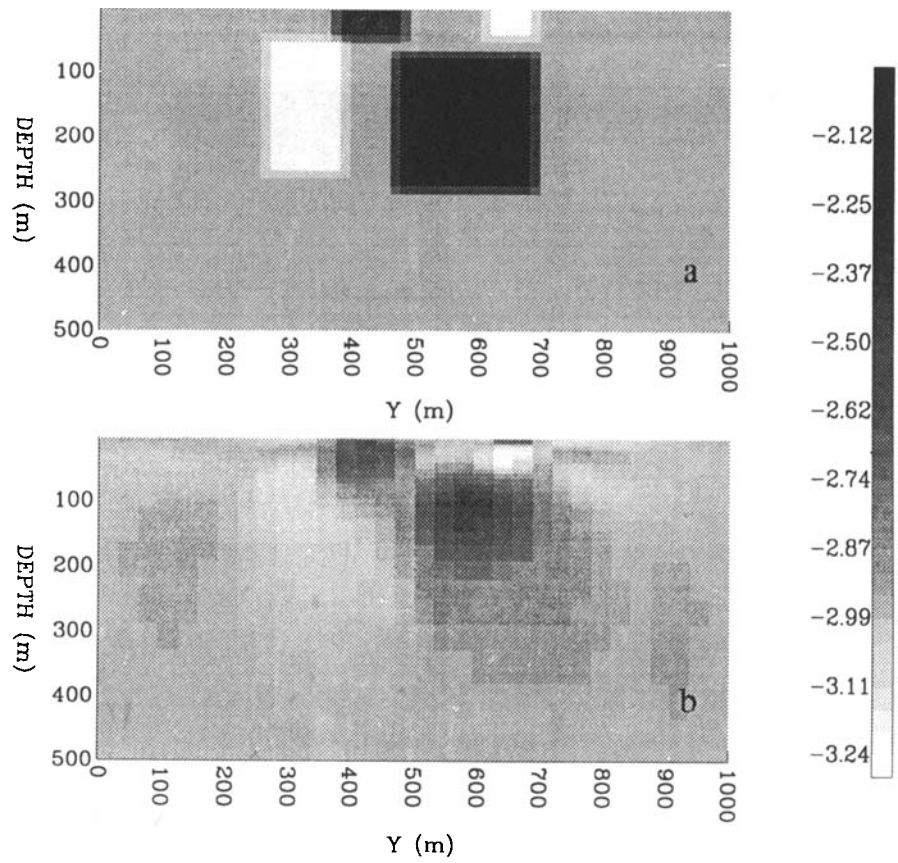


Figure 10. The comparison of the true model (a) and the recovered model (b) in the section $x = 450$ m (scale in $\log_{10} \sigma$).

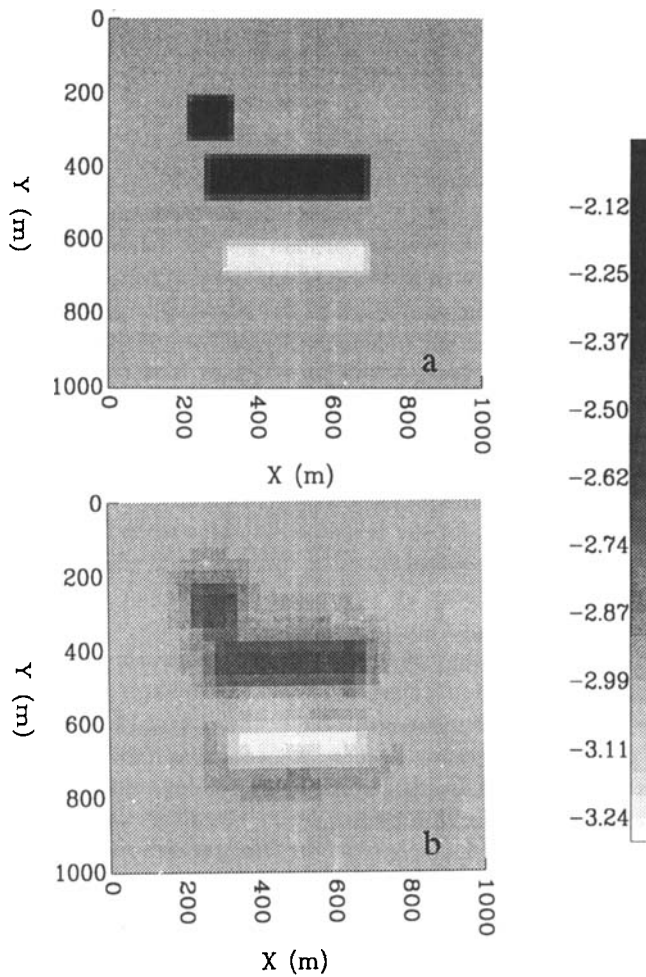


Figure 11. The comparison of the true model (a) and the recovered model (b) at depth of 30 m (scale in $\log_{10} \sigma$).

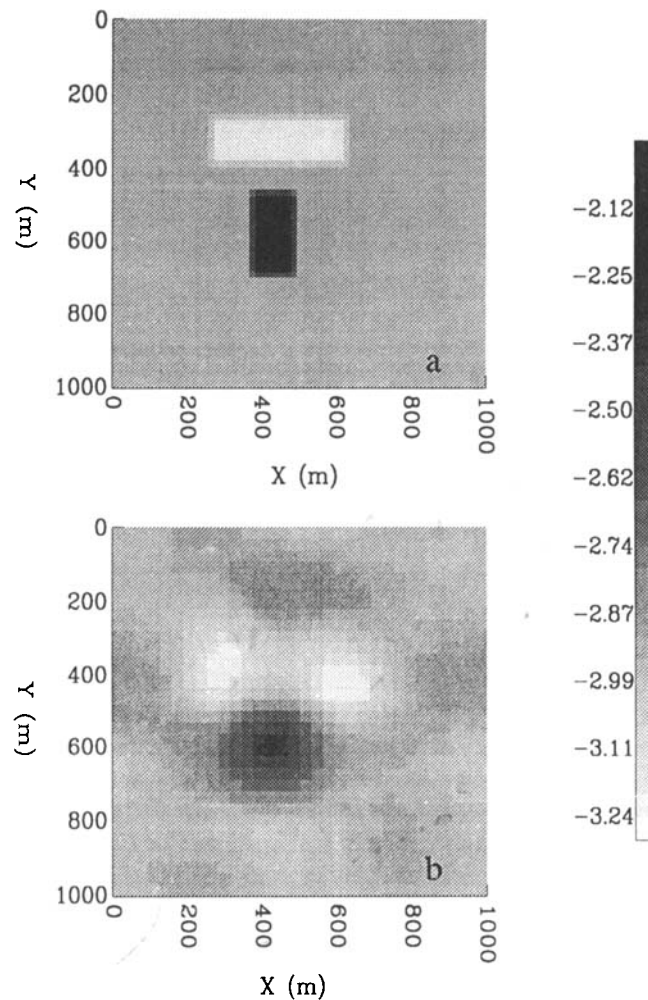


Figure 12. The comparison of the true model (a) and the recovered model (b) at depth of 150 m (scale in $\log_{10} \sigma$).

the assumption that the surface conductivity be constant and the conductivity deviation is small. Even with such violations in the model, the algorithm still recovers the model reasonably well. This shows that the algorithm is quite robust.

As a second example, we have inverted a set of field data. The data are collected from an E-SCAN survey designed to assist exploration for certain types of epithermal deposits. Epithermal deposits typically occur in the region with well-developed fracture and fault systems. Existing faults or fractures act as feeders of hot fluid which alters the host rock and deposits minerals. Ore deposits are often associated with silicifications with depth 'roots', which tend to produce resistive anomalies in the DC resistivity experiments. Therefore, the E-SCAN survey is employed in this area in an attempt to map such silicification zones and fault structures.

The original data were taken over a 32×5 grid with 91.44 m spacing. 26 pole-pole apparent resistivity maps in x - and y - and diagonal directions are gathered for the inversion. A value of $18 \Omega \text{ m}$ is estimated for the background resistivity. As an illustration, Fig. 13 shows one cross-section from the inverted conductivity model. The section is taken from the conductivity model directly beneath the original area of field experiment. Similar to the synthetic example, the recovered conductivity model has many structural details at shallow depth but becomes increasingly smooth at greater depth.

The model exhibits clear definitions of conductive and resistive units. The large resistive feature (near $x = 1800 \text{ m}$) may conform with the general pattern of silicified structures in epithermal deposits, which frequently expand upward near the surface to become cone-like or mushroom-shaped. Ideally, this 3-D conductivity model should be compared with known geologic information to verify its validity. Although five major lithologic units have been identified in this region, their geo-electric properties are still uncertain. No borehole information is available for such verification. Thus we can mainly assess the result from the viewpoint of algorithm performance. The RMS misfit to the observed data by the best fitting half-space model is 57 per cent. The resultant conductivity model from the inversion reduces the misfit to 28 per cent. This indicates that the algorithm has taken a first step towards producing an acceptable model. Due to the nature of the algorithm, there is little chance that large-scale spurious structures will be introduced. These facts suggest that the observed features in the inversion image may reflect true large-scale conductivity variations.

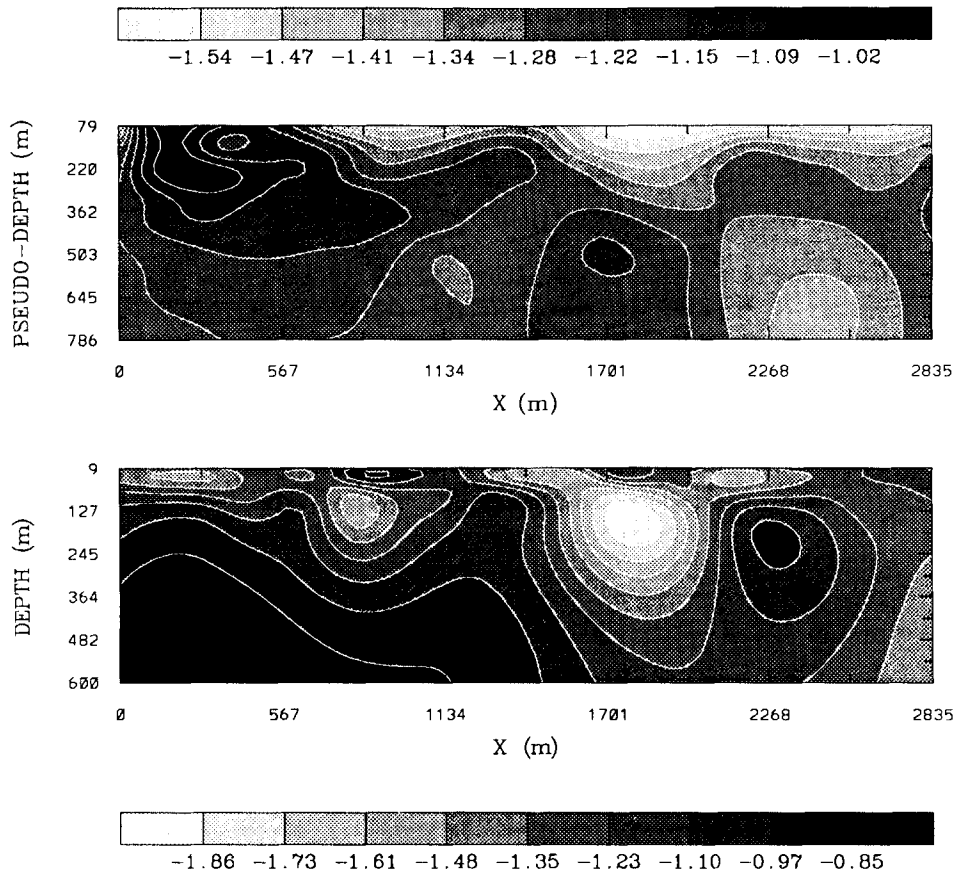


Figure 13. One slice from the conductivity model (b) recovered by inverting a field data set and the apparent conductivity pseudo-section (a) in the same section (scale in $\log_{10} \sigma$).

DISCUSSION

Three different algorithms have been developed to image or invert the subsurface conductivity structures. All algorithms are based upon the Born approximations of the DC potential responses and the explicit use of E-SCAN data set. It has been shown that the Born approximation provides a reasonable representation of the true potential, especially in 3-D cases. Thus it is viable to image or invert for subsurface structures using such an approximation.

For 2-D models, the first approach is to image the boundary of subsurface structures using the accumulated charge density. The secondary potential is produced by the accumulated charges on the subsurface boundaries and consequently the recovery of the charge density effectively images these boundaries. Linear programming techniques are employed to invert the secondary potentials for a sparse representation of the charge density due to each of the current sources. The composite of these images yields a relatively complete image for simple subsurface structures. The algorithm has worked satisfactorily for simple models. However, the difficulty lies in combining a final result from several independent inversions. This can be unstable.

To overcome the difficulties encountered in the charge density imaging, a direct formulation is developed which inverts approximately for simple 2-D conductivity structures. The algorithm also employs linear programming techniques for the inverse solution. An approximate conductivity model is constructed which satisfies all the available data. The method works well for relatively simple structures. For smallest l_1 model construction, the algorithm is very efficient. As the component of variation increases, the algorithm becomes slower due to the linear programming solution. Because of the approximations involved, the semiquantitative result mostly serves as an image representation of the model. In general, the approximation is severe in the 2-D cases, especially with the complicated structures where the total field deviates greatly from the background field. Consequently, the inversion by this approach may be less appealing in practice.

For 3-D models, an approximate inversion algorithm has been developed based upon the integral equation for surface pole-pole apparent resistivity data. The algorithm is designed to work for general 3-D models composed of perturbations to a background conductivity. Synthetic examples show that it can handle fairly large conductivity contrasts and, to a certain

degree, surface variations. The approach we have taken has some general implications. The algorithm can be viewed from different aspects. By applying a linear operator (2-D Fourier transform) to the basic data equation, the 3-D inverse problem is broken into a set of independent 1-D inverse problems. Each 1-D problem can be solved easily and efficiently. This results in an algorithm which is much more efficient than solving the original problem directly. From the view point of inversion, this approach also has merits. The Fourier transform separates the large-scale features (low-wavenumber components) and small-scale features (high-wavenumber components) in the data. Features of different scales are fit by finding the model components of corresponding scales. Thus the horizontal variability in the conductivity can be easily controlled by the largest wavenumber included in the inversion. This process makes the inversion very stable.

The success with synthetic models, and the geologic reasonableness of the result from the 3-D algorithm applied to field data, provide a base for optimism for the approximate inversion. The next step of the research will be to input the recovered conductivity model into a full 3-D forward modelling algorithm to quantify the misfit between observed and predicted data. The approximate inverse mapping can then be incorporated into an iterative algorithm to yield a quantitative and rigorous solution to the 3-D resistivity problem.

ACKNOWLEDGMENTS

The authors wish to thank S. E. Dosso and R. G. Ellis for many helpful discussions. Dr R. G. Ellis's expertise in numerical computing has been very valuable to this work. This research is supported by NSERC CRD grant 5-80141 and Premier Geophysics. YL is partly supported by a University of British Columbia Graduate Fellowship.

REFERENCES

- Alfano, L. M., 1959. Introduction to the interpretation of resistivity measurements for complicated structural conditions, *Geophys. Prosp.*, **7**, 311–368.
- Backus, G. E. & Gilbert, J. F., 1967. Numerical application of a formalism for geophysical inverse problems, *Geophys. J. R. astr. Soc.*, **13**, 247–276.
- Boerner, D. E. & West, G. F., 1989. Frechet derivatives and single scattering theory, *Geophys. J. Int.*, **98**, 385–390.
- Bracewell, R. N., 1978. *The Fourier Transform and its Applications*, McGraw-Hill, New York.
- Dosso, S. E. & Oldenburg, D. W., 1989. Linear and non-linear appraisal using extremal models of bounded variation, *Geophys. J. Int.*, **99**, 483–495.
- Edwards, L. S., 1977. A modified pseudosection for resistivity and IP, *Geophysics*, **42**, 1020–1036.
- Kaufman, A. A., 1985. Distribution of alternating electrical charges in a conducting medium, *Geophys. Prosp.*, **33**, 171–184.
- Li, Y. & Oldenburg D. W., 1991. Aspects of charge accumulation in dc resistivity experiments, *Geophys. Prosp.*, **39**, 803–826.
- Murty, K. G., 1983. *Linear Programming*, Wiley, New York.
- Oldenburg, D. W., 1984. An introduction to linear inverse theory, *IEEE Trans. Geosci. Remote Sensing*, **GE-22**, 665–674.
- Parker, R. L., 1977. Understanding inverse theory, *Ann. Rev. Earth planet Sci.*, **5**, 35–64.
- Snyder, D. D., 1976. A method for modelling the resistivity and IP responses of two dimensional bodies, *Geophysics*, **41**, 997–1015.